Final Technical Report

External Grant Award Numbers: G12AP20027 and G12AP20025

Title: Structure, Seismicity, and Stress along the San Andreas Fault near SAFOD: Collaborative Research with UW-Madison and Georgia Tech

Investigators:

Clifford Thurber
University of Wisconsin-Madison
1215 W. Dayton St.
Madison, WI 53706
Phone: (608) 262-6027, FAX: (608) 262-0693
thurber@geology.wisc.edu

Zhigang Peng
Georgia Institute of Technology
311 Ferst Drive
Atlanta, GA, 30332-0340
Phone: (404) 894-0231, Fax: (404) 894-5638
zpeng@gatech.edu

Term Covered by the Report: January 1, 2012 - December 31, 2013

Funding expended: $53,337 (UW, G12AP20027), $50,656 (GT, G12AP20025)

Structure, Seismicity, and Stress along the San Andreas Fault near SAFOD:
Collaborative research with UW-Madison and Georgia Tech

Investigations undertaken

The San Andreas Fault Observatory at Depth (SAFOD) has yielded significant new insights into the nature of the San Andreas fault (SAF). In particular, the recovery of ~40 meters of core containing two meter-thick zones of fault gouge and adjacent zones of damage and alteration provides a unique opportunity to characterize the physical and chemical properties of fault zone rocks from a depth where earthquakes occur, although these samples are interpreted to come from a creeping, not seismogenic, part of the fault (Hickman et al., 2007, 2008). We have been working to improve our understanding of the context within which these fault zone samples existed *in-situ* by utilizing arrival times of fault zone head waves (FZHW's) and the associated direct-wave secondary arrivals (DWSA's) to improve the seismic tomography image of the SAF at relatively fine scale.

FZHW's have been used previously to constrain fault zone velocity contrasts along the SAF system based on the relative move-out of FZHW's versus DWSA's (Ben-Zion and Malin, 1991; Ben-Zion et al., 1992; McGuire and Ben-Zion, 2005; Lewis et al., 2007; Zhao and Peng, 2008; Zhao et al., 2010). Our project takes the next step in modeling FZHW and DWSA arrival times by incorporating them in a formal tomographic inversion for three-dimensional (3D) seismic velocity structure, building on the work of Thurber et al. (2006) and Zhang et al. (2009). We take advantage of the dense surface and borehole seismic instrumentation around the study region, capitalize on the extensive FZHW analysis results of Zhao et al. (2010), and incorporate previously unavailable temporary array data to improve the delineation of the seismically active structures. We obtain an updated tomographic model in which the velocity contrast across the SAF is markedly sharpened compared to the previous case when these observations were not included. In particular, we find that the inclusion of FZHW and DWSA arrivals results in as much as a 10% increase in the across-fault velocity contrast for the P-wave velocity model at Parkfield. Viewed along strike, three pronounced velocity contrast regions are observed: a pair of strong positive velocity contrasts (SW side of the fault is fast), one NW of the 1966 Parkfield earthquake hypocenter and the other SE of the 2004 Parkfield earthquake hypocenter, and a strong negative velocity contrast (NE side of the fault is fast) between the two hypocenters. The negative velocity contrast area largely overlaps the zone of peak coseismic slip estimated in several slip models for the 2004 earthquake, suggesting the negative velocity contrast played a role in defining the rupture patch of the 2004 Parkfield earthquake. Following Ampuero and Ben-Zion (2008), the pattern of velocity contrasts is consistent with the observed bilateral rupture propagation for the 2004 Parkfield earthquake.

We also obtain measurements of the arrival azimuth angles of FZHW's and DWSA's, and assess the utility of such observations for further constraining fault zone structure. Unfortunately, our observations suggest that while particle motions could be used to demonstrate the polarizations of the FZHW and direct P waves for some events, they are not reliably observed for all source-receiver pairs. Furthermore, we conclude that the non-localized sensitivity of arrival azimuth data to velocity model perturbations along the ray path means that the azimuth information cannot provide effective constraints on the 3D structure.

Accomplishments

Large crustal faults such as the SAF typically juxtapose rocks of significantly different elastic properties, resulting in a well-defined across-fault material contrast. A sharp material contrast across the fault interface is expected to generate FZHW's that spend a large portion of their propagation paths refracting along the interface (Ben-Zion, 1989, 1990; Ben-Zion and Aki, 1990). The FZHW's propagate with the velocity of the faster block, and are radiated from the fault to the lower velocity block where they are characterized by an emergent waveform with opposite first-motion polarity to that of the DWSA's. Since FZHW's spend most of their propagation paths along the fault interface, they provide a high-resolution tool for imaging the velocity contrast across major crustal faults (Ben-Zion and Malin, 1991; Ben-Zion et al., 1992; McGuire and Ben-Zion, 2005; Lewis et al., 2007; Zhao and Peng, 2008; Zhao et al., 2010; Bulut et al., 2012; Allam et al., 2014).

We find that the inclusion of FZHW's and DWSA's results in as much as a 10% increase in the across-fault velocity contrast for the Vp model at Parkfield relative to the model of Thurber et al. (2006). In the following sections, we describe how we have included FZHW and DWSA arrival times in a formal inversion for 3D P-wave velocity structure. We discuss the resulting model, including comparisons to the Vp model of Thurber et al. (2006) and the across-fault velocity contrasts estimated by Zhao et al. (2010). Further comparison is made between the velocity model contrasts determined here and the spatial extent of coseismic slip for the 2004 Parkfield earthquake. Finally, we compare expected rupture propagation directions for the 1966 and 2004 Parkfield earthquakes based on the relationship between the velocity contrasts and the observed rupture propagation directions for the two events.

Background

Zhao et al. (2010) systematically analyzed large datasets of near-fault waveforms recorded by several permanent and temporary seismic networks along the Parkfield section of the SAF. They found clear FZHW's at many stations on the NE side of the SAF near the San Andreas Fault Observatory at Depth (SAFOD), indicating the presence of a sharp across-fault material contrast in that region. Based on the systematic move-out between the FZHW's and associated DWSA's, they estimated an average P-wave velocity (Vp) contrast of about 5-10%. In comparison, the FZHW is not clearly developed along the SAF near Gold Hill (GH), located near the 2004 Parkfield earthquake epicenter, and the average Vp contrast there is estimated as 0-2%. The weak evidence for FZHW's and the inferred negligible velocity contrast near GH are consistent with geophysical observations and geological interpretations of a sliver of high-velocity rock immediately to the NE of the SAF near Gold Hill (McLaughlin et al., 1996) and previous 3D seismic tomography results showing such a high-velocity feature (Eberhart-Phillips and Michael, 1993; Thurber et al., 2004, 2006). This is also consistent with a recent study of statistically preferred southeast rupture propagation for microearthquakes in this region (Lengliné and Got, 2011), supporting the concept that across-fault material contrast can provide an important control on the earthquake rupture propagation direction (Andrews and Ben-Zion, 1997; Ampuero and Ben-Zion, 2008).

The local-scale tomography study of Zhang et al. (2009) for a roughly 10 km^3 volume centered on SAFOD and the more regional-scale study of Thurber et al. (2006) for a 130 km x 120 km x 20 km volume centered on the 1966 Parkfield earthquake rupture provide what are probably the best 3D images of the seismic velocity structure of the area (Figure 1). The former shows a low velocity zone associated with the SAF extending as deep as 7 km near SAFOD, and both image the well-known velocity contrast across the fault. In this report, we present a model of 3D velocity structure for the Parkfield region that utilizes a combination of existing P-wave arrival time data, including FZHW's, plus new DWSA and FZHW data.

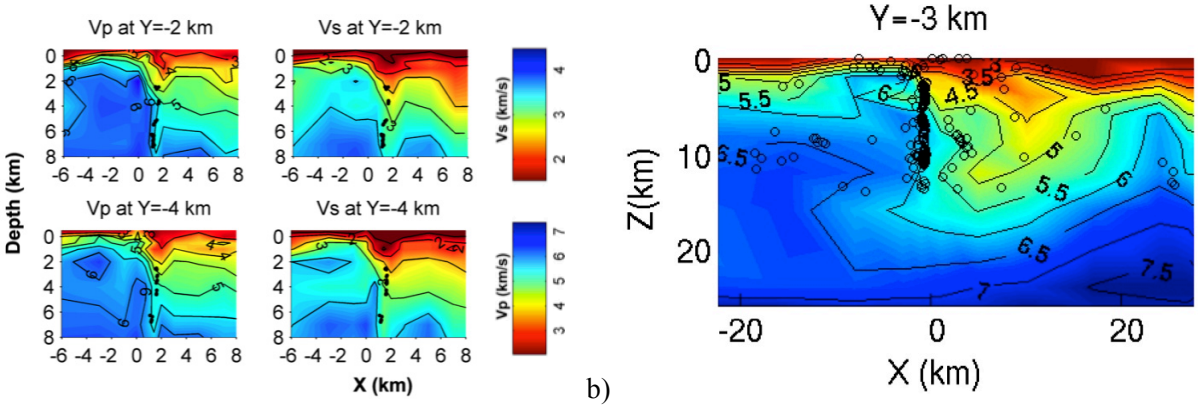

Figure 1. (a) Representative cross-sections through the local scale 3D Vp and Vs models of Zhang et al. (2009) near SAFOD (which is located at X=0, Y=0 in this model) showing a deeply penetrating LVZ along the SAF. (b) Portion of a representative cross-section through the regional scale 3D Vp model of Thurber et al. (2006) centered on Parkfield, showing the well known velocity contrast across the SAF, with the SW side faster. For this model, the coordinate origin is at Middle Mountain.

Thurber et al. (2006) also studied in detail the spatial distribution of seismicity along and near the 2004 Parkfield earthquake rupture. Their study confirms the predominance of streaks and clusters in the pattern of seismicity as viewed along fault strike (Figure 2), as was previously reported by Waldhauser et al. (2004), but now including the 2004 aftershocks. The overlap between the background seismicity and the 2004 aftershocks is remarkable, and this overlap appears to extend all the way back to the 1966 aftershocks (Thurber et al, 2006). Thus these streaks and clusters are stable features that have survived for more than an entire earthquake cycle, demonstrating that the patches that fail as aftershocks (and also as background earthquakes) require no special process specifically related to the main shock (e.g., transient fluid flow or stress changes) in order to occur, although their temporal occurrence patterns do show clear correlations with the main shock (Legliné and Got, 2011).

Research accomplished - arrival time tomography

We have developed a model of the 3D velocity structure for the Parkfield region that utilizes a combination of arrival times for FZHW's and the associated DWSA's as well as existing P-wave arrival time data. Arrival time picks were made manually for earthquakes recorded at Parkfield between 1984 and 2006 on the Parkfield Area Seismic Observatory (PASO) array, UC-Berkeley High Resolution Seismic Network, USGS Central California Seismic Network, and USGS temporary stations (Figure 3). Existing P-wave absolute and differential time data as well as cross-correlation data were from Thurber et al. (2006) and Zhang et al. (2009). The catalog of FZHW and DWSA picks was from Zhao et al. (2010). Catalog differential times were calculated from this data set.

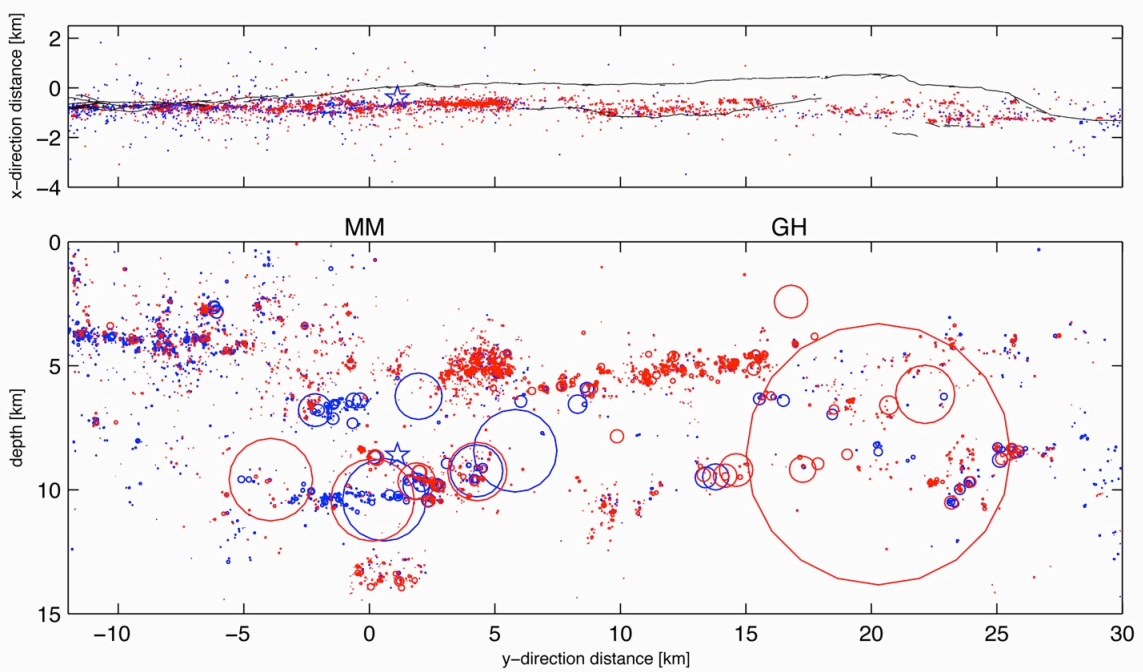

Figure 2. (top) Map view and (bottom) along-fault cross-section of DD-relocated seismicity along and northwest of the 2004 Parkfield rupture zone, covering the time period 1984-2005. The blue star is the 1966 main shock hypocenter. Blue circles are events from 1984 to the 2004 main shock, and red circles are the 2004 main shock and its aftershocks. In the cross section, circles indicate size of a model circular source with a 30 bar stress drop. From Thurber et al. (2006).

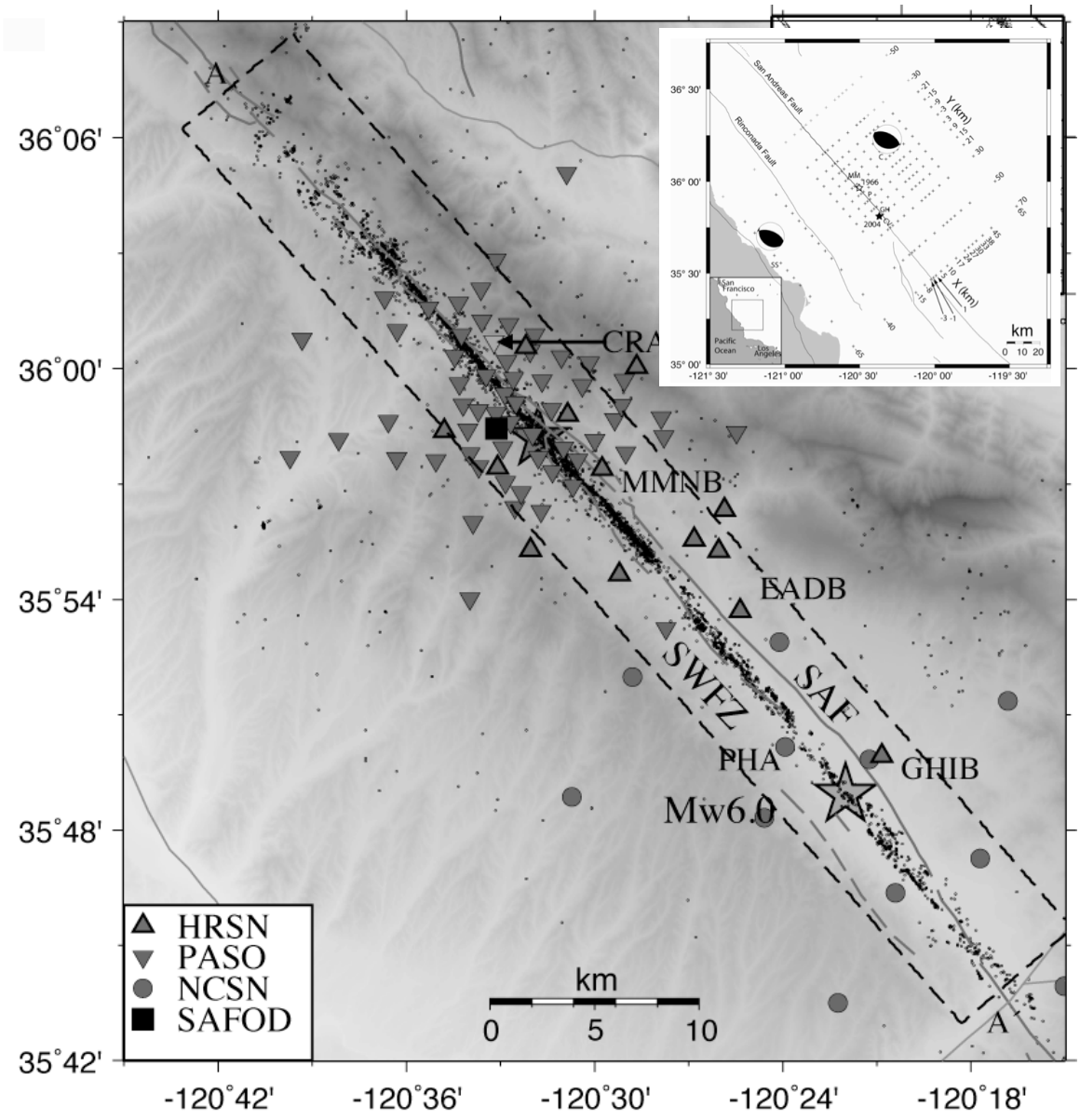

Figure 3. Dataset for our inversion, with station symbols as indicated, earthquakes as small black dots, and the location of SAFOD shown by the black square. The inset shows the X-Y coordinates and the inversion grid used by Thurber et al. (2006), which was modified for our work.

We have modified the double-difference tomography algorithm tomoDD (Zhang and Thurber, 2003) to incorporate FZHW and associated DWSA times into a formal inversion for Vp structure. We have adapted the pseudo-bending method of Um and Thurber (1987) to compute travel times for both the first-arriving FZHW's and the later arriving DWSA's. The pseudo-bending method relies on the fact that for a true ray path satisfying the ray equations, the ray curvature (vector of the second spatial derivative along the path) is everywhere anti-parallel to the component of the velocity gradient normal to the ray path. The pseudo-bending strategy involves locally perturbing an approximate initial ray path (determined from a brute-force search among a "web" of arcuate paths of varying dip and curvature) so that the eikonal equation is satisfied in a piecewise manner, and iterating to convergence. The method has proven to be extremely effective when path lengths are up to ~60 km in length, with accuracies comparable to the

finite-difference method (Haslinger and Kissling, 2001). The strategy for finding secondary arrivals using pseudo-bending is relatively simple. For a DWSA arrival, we force pseudo-bending to derive the direct path instead of the first-arriving FZHW path by restricting the starting path to the vertical plane connecting the earthquake and station and artificially reducing the velocities on the southwest side of the SAF. The pseudo-bending algorithm will thus converge to what is a local-minimum DWSA path instead of the global minimum FZHW path.

The grid used in this study (Figure 3 inset) is modified from Thurber et al. (2006). Their nodes at X = -3, -1, and 1 km are repositioned to X = -1.75, -0.75, and 0.25 km so that the shifted nodes fall within and immediately adjacent to the seismicity along the fault. Initially, even finer near-fault node spacing was attempted (0.5 km node spacing within 2 km of the fault in the X-direction). However, checkerboard tests revealed that such fine model parameterization near the fault zone yielded poor recovery within this region. Thus, the coarser near-fault model parameterization noted above was used for the spacing of nodes in the X-direction. Since additional data from the local study of Zhang et al. (2009) were incorporated, we have created a finer grid near SAFOD by also adding nodes at Y = -6, 0, 6, and 12 km. We obtained a starting model by inverting the existing P-wave data of Thurber et al. (2006) and Zhang et al. (2009) using the modified grid. We also included the FZHW times of Zhao et al. (2010). The Vp model of Thurber et al. (2006), interpolated onto the modified grid, is used as the initial model for that step. The DWSA times of Zhao et al. (2010) were then incorporated into the dataset and the inversion was carried out to produce the final Vp model.

The new 3D Vp model for the Parkfield region is presented here in selected fault-normal cross-sections (Figure 4a-f). For the displayed cross-sections, top panels represent the starting model, middle panels represent perturbations to the starting model, and bottom panels represent the final Vp model with DWSA times incorporated. We estimate the Vp model quality using a combination of a synthetic recovery test and the derivative weight sum (DWS) distribution. The DWS parameter reflects the density of rays passing near a grid node, where weighting is calculated based on each ray's distance from a particular grid node (Toomey and Foulger, 1989; Thurber and Eberhart-Phillips, 1999). The DWS value of 200 corresponds to areas in the synthetic model that are well recovered in checkerboard tests.

The inclusion of the DWSA times increases the overall number and density of ray paths sampling the fault zone. The resulting Vp model shows an increase in the across-fault velocity contrast relative to the starting model (Figure 4). Overall, contours of high and low velocity on opposite sides of the fault move to align nearer to and/or along zones of seismicity, yielding an overall increase in the across-fault velocity contrast. Cross-sections NW of the 1966 Parkfield earthquake hypocenter (Figure 4a-b: Y = -21 and -15 km; Z = 3 to Z = 10 km) show the 5.5 and 6 km/s contours moving to align nearer to and along the seismicity. The > 6 km/s values seen here on the SW side of the seismicity are representative of the high-Vp rocks of the Salinian block (Thurber et al., 2006). Vp values decrease to as low as 3 to 4 km/s moving NE of the seismicity, likely representing Great Valley sequence rocks. Between the 1966 and 2004 Parkfield earthquake hypocenters (Figure 4c-d: Y = 3 and 6 km; Z = 5 to 15 km), Vp values SW of the seismicity slightly decrease to 6.0 km/s and values NE of the seismicity increase to ~6.6 km/s with a maximum value of 7.3 km/s. This yields a reversal in the across-fault velocity contrast relative to that found NW of the 1966 hypocenter. In this case, we have high-velocity rocks on both sides of the fault with the faster material lying NE of the seismicity. Figure 4c-d show that the faster material is ~2 km thick in the X-direction, and Figure 5 shows the across-fault reversal in velocity contrast extending from Y = 0 to 15 km. Checkerboard tests demonstrate that a feature of this thickness, extending from Y = 0 to 15 km, is well recovered for $Z \leq 12$ km, indicating that the higher velocity feature and corresponding reversal in the across-fault velocity contrast are robust results. Eberhart-Phillips and Michael (1993) and Thurber et al. (2006) noted this reversal with Thurber et al. (2006) observing a maximum value of 6.6 km/s for Vp on the NE side of the seismcity. Vp values observed NE of the seismicity in this study and Thurber et al. (2006) are too high to be associated with the Salinian block. Thurber et al. (2006) suggest this fast region is associated with the high Vp greenstones and mafic rocks of the Permanente Terrane. Brocher (2008) estimated a Vp of ~6.9 km/s and ~6.7 km/s for mafic and greenstone rocks of northern California, which fits well with values observed in our study.

Near and to the SE of the 2004 hypocenter (Figure 4e-f: Y = 21 and 30 km; Z = 5 to 12 km), the velocity contrast reverts back to the pattern seen NW of the 1966 hypocenter, where Vp values SW of the seismicity are higher than those to the NE. Again we see the 6 km/s contour on the SW side moving to align along the seismicity, with maximum Vp values of 6.4 km/s immediately SW of the seismicity. In approximately the same region, Thurber et al. (2006) show a maximum Vp of ~6 km/s. NE of the seismicity; the high velocity body previously observed at Y = 6 km has migrated farther NE, and an area of lower Vp (5.5 to 6 km/s) separates it from the seismicity, as also seen in Thurber et al. (2006).

The location of seismicity near the SAF trace suggests that the active fault surface falls near X = -0.75 km. To quantify the across-fault velocity contrast, the difference is taken between Vp model values immediately SW (at X = -1.75 km) and NE (at X = 0.25 km) of the seismicity. Figure 5 a-d show the across-fault velocity contrast of Thurber et al. (2006), the starting Vp model used in this study, and the change in Vp and the final Vp model with DWSA times included, respectively. The across-fault velocity contrast in our starting model differs from the final model of Thurber et al. (2006) by as much as 5% due to the change in gridding and inclusion of additional FZHW data. For the central portion of the starting model (Y = -6 to 12 km), incorporation of Zhang et al.'s (2009) dataset also influences the starting model.

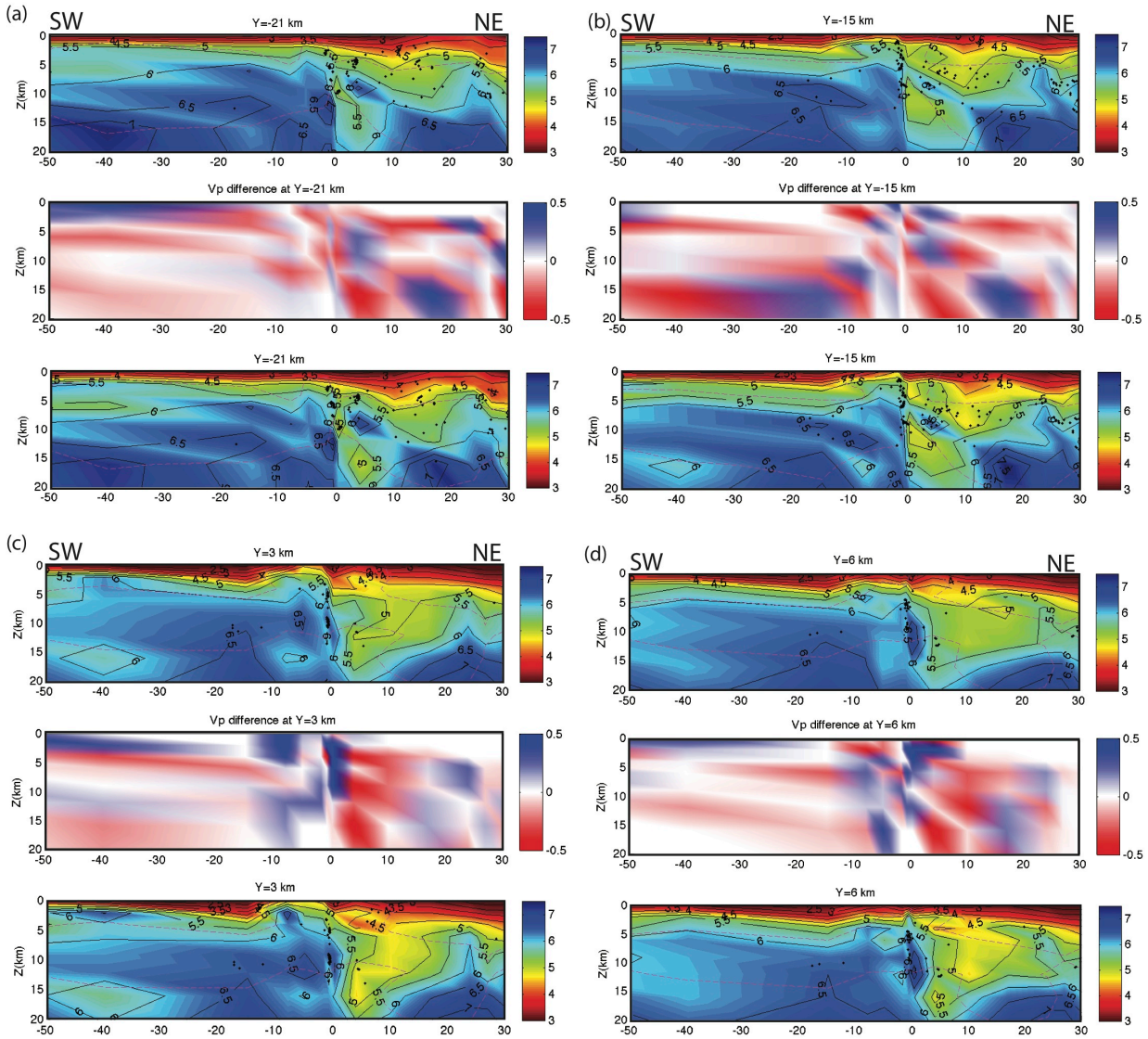

Figure 4 (continued)

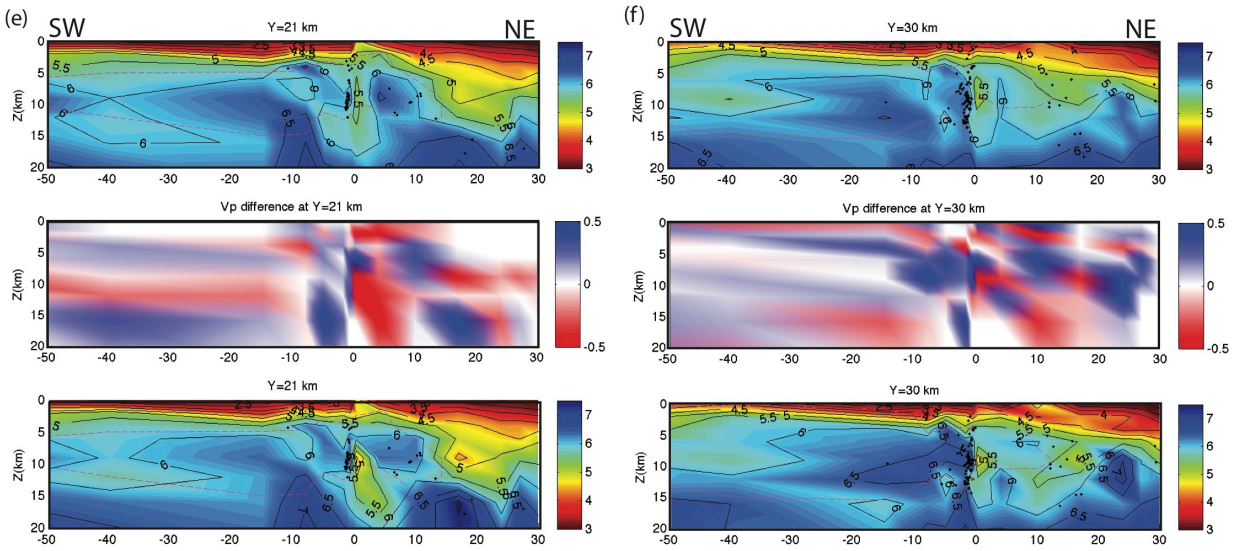

Figure 4. Selected fault-normal cross-sections from the inversion. Dashed lines represent well-resolved regions of the model (DWS values > 200). Black dots are earthquake hypocenters used in velocity inversion. Top panels are the starting model, middle panels represent perturbations to the starting model, and bottom panels are the final velocity inversion results with DWSA times incorporated. Vp is shown in km/s. Distance on the horizontal axis is in km, with 0 corresponding to the SAF at the estimated 1966 Parkfield earthquake's epicenter. From Bennington et al. (2013).

We observe that inclusion of DWSA data increases the amplitude of the across-fault velocity contrasts (both negative and positive; Figure 5d) by as much as 5% relative to the starting model (Figure 5c) and as much as 10% relative to Thurber et al. (2006). In addition, the DWSA-constrained Vp model produces velocity contrast regions that extend farther along the fault than for the starting model (Figure 5b) or Thurber et al. (2006) (Figure 5a).

For the three models shown in Figure 5, we observe a positive velocity contrast NW of the 1966 hypocenter, a striking negative velocity contrast between the hypocenters of the 1966 and 2004 Parkfield earthquakes, and a positive across-fault velocity contrast to the SE of the 2004 hypocenter. Figure 5d shows the positive velocity contrast NW of the 1966 hypocenter to be an elongate feature extending from immediately NW of the 1966 hypocenter to nearly Y = -40 km and having contrast values as large as 20%. Zhao et al. (2010) used move-out curves between first arriving FZHW and later arriving DWSA to estimate the across-fault velocity contrast in this region and found a maximum value of ~20%, which agrees well with our results. Adjacent to this region, there is a strong, negative velocity contrast (as large as -18%) present from Z = 7 to 15 km depth and Y = -2 to 15 km. Due to the spatial distribution of stations and local seismicity, Zhao et al. (2010) had difficulty resolving the value of a negative velocity contrast in this region.

Thurber et al. (2006) noted a possible spatial relationship between this region and the coseismic slip associated with the 2004 Parkfield earthquake. We compare a suite of coseismic slip models for the 2004 Parkfield earthquake determined via geodetic and/or strong motion data (Kim and Dreger, 2008; Custódio et al., 2009; Barnhart and Lohman, 2010; Bennington et al., 2011) to the negative velocity contrast area. Contours of peak coseismic slip (≥ 0.3 m) are overlain on the Vp contrast determined in this study (Figure 6). A strong correlation is observed between the lateral extent of the main slip patch of the slip models and the negative velocity contrast seen in our model, although the depth ranges differ: peak slip in three of these coseismic slip models extends from 5 to 10 km depth while the main negative velocity contrast exists from 7 to 15 km. Interestingly, the two main patches of peak slip seen in the coseismic slip model of Kim and Dreger (2008) (Figure 6; white dashed line) are located within the main negative velocity contrast and a smaller negative velocity contrast centered at Y = 22 km and Z = 12 km. This suggests that

the negative velocity contrast observed here played a role in defining the rupture patches for the 2004 Parkfield earthquake.

SE of the 2004 hypocenter, Zhao et al. (2010) observe a sparseness of FZHW's and infer an absent or very small velocity contrast. For the same region, we observe a velocity contrast at Z ≤ 3 km of -5 to -15% and, immediately below this, a positive velocity contrast of 5 to 15% at Z = 5 to 12 km. Zhao et al. (2010) suggest that the propagation of FZHW's through regions of varied velocity contrasts could reduce the velocity contrast values they obtain. Thus, the juxtaposition of the high negative and high positive velocity contrasts in this region could be responsible for a lack of observable FZHW's.

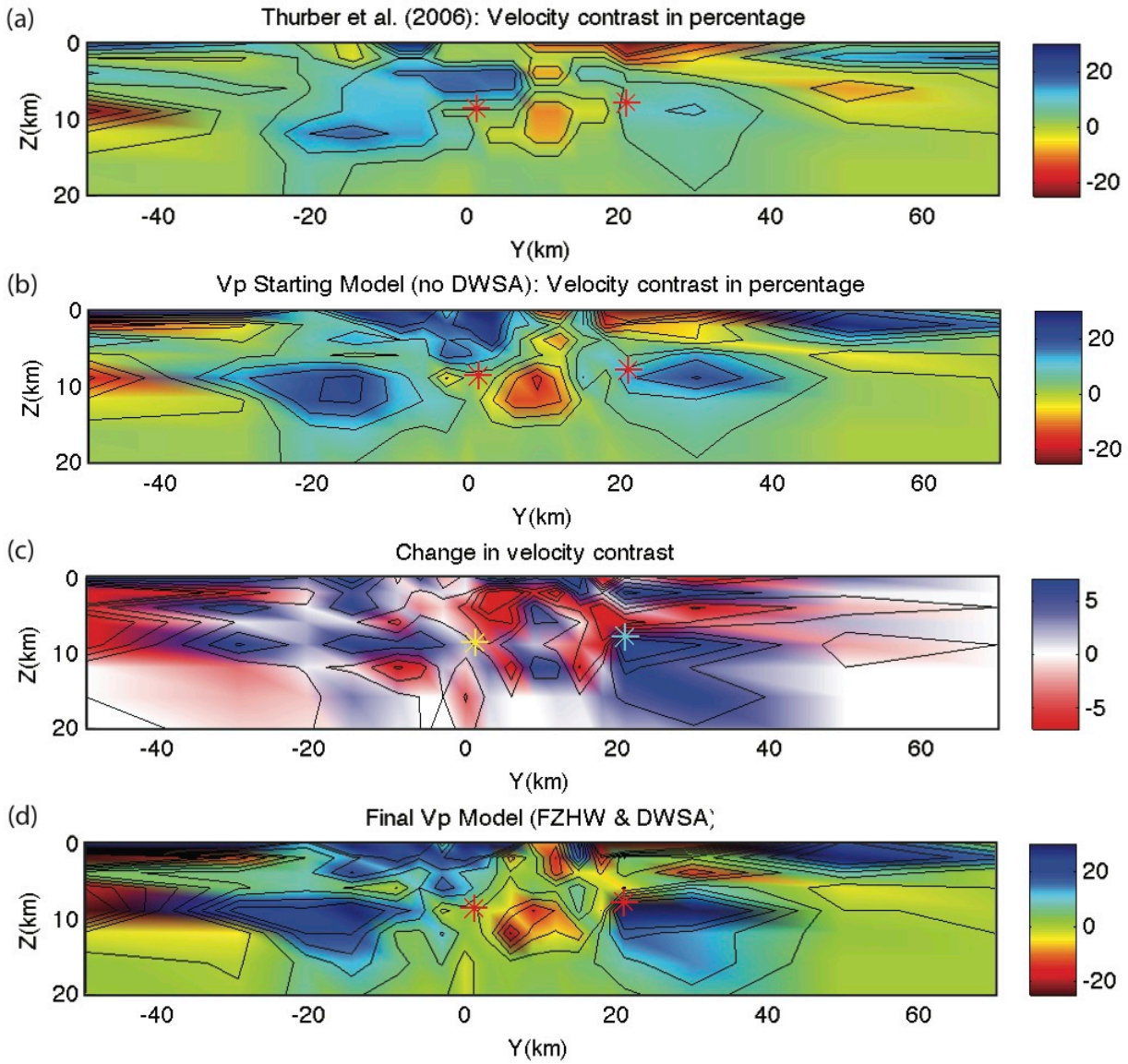

Figure 5. (a) The across-fault velocity contrast for the Vp model of Thurber et al. (2006). (b) Velocity contrast across the fault for our starting model for which DWSA data were excluded. (c) Perturbations to the starting model when DWSA data were incorporated. (d) The across-fault velocity contrast for the Vp model when DWSA data were incorporated. Left and right stars indicate the 1966 and 2004 Parkfield earthquake hypocenters. The across-fault velocity contrast wss calculated by differencing node values immediately adjacent to the seismicity, i.e., X = -1.75 km minus X = 0.25 km velocity values. From Bennington et al. (2013).

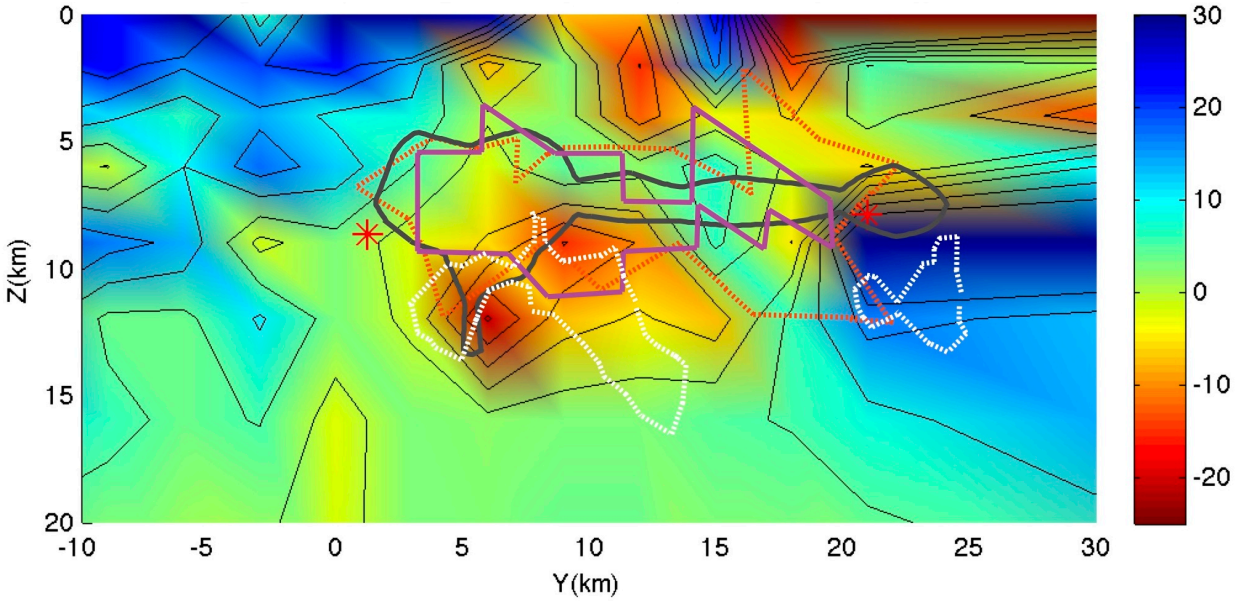

Figure 6. Vp across-fault velocity contrast incorporating all first arriving P-waves and DWSA's, shown as the colored model with black contour lines (in percent). Overlain solid grey, dashed white, solid magnenta, and dashed red lines represent the > 0.3 m slip contour of the coseismic slip models of Custódio et al. (2009), Kim and Dreger (2008), Bennington et al. (2011), and Barnhart and Lohman (2010), respectively. From Bennington et al. (2013).

Harris and Day (2005) examined magnitude 6 earthquakes that occurred in Parkfield in 1934, 1966, and 2004 together with several magnitude 4 to 5 earthquakes. Based on numerical simulations, they suggested that the bimaterial interface is an unlikely predictor of rupture propagation direction. Ben-Zion (2006) argued that the eight magnitude 4 to 6 Parkfield earthquakes examined by Harris and Day (2005) were small to moderate in size, suggesting the events could be controlled by local structural complexities. In additional, the total number of events examined was not statistically significant. Nevertheless, if we assume rupture direction is controlled by the bimaterial interface (Ampuero and Ben-Zion, 2008), we can use the velocity contrasts in Figure 5 for "prediction" of the preferred rupture propagation directions of the 1966 and 2004 Parkfield earthquakes. The 2004 Parkfield earthquake is located between a large, positive velocity contrast to the SE and a large, negative velocity contrast to the NW. Following Ampuero and Ben-Zion (2008), the positive velocity contrast suggests a preferred propagation direction to the SE whereas the negative velocity contrast suggests a preferred propagation direction to the NW. Taken together, this suggests bilateral rupture propagation as was observed during the 2004 Parkfield earthquake. The velocity contrasts of opposing sign abutting the 1966 Parkfield earthquake would suggest bilateral rupture in a similar manner. However, the predominantly velocity-strengthening behavior of the creeping section of the SAF would prevent rupture to the NW. Thus, it is not surprising that rupture propagated only to the SE during this event.

Finally, we note that Zhao et al. (2010) picked FZHW's and DWSA's based only on their waveform characteristics (emergent vs. sharp) and opposite polarities. The method of Bulut et al. (2012) used an additional constraint based on differences in the azimuths of FZHW's and DWSA's and would, therefore, result in more reliable phase picks. Our imaging resolution could be improved further by using more accurate picks through the method of Bulut et al. (2012) and/or other methods.

Research accomplished - polarization (arrival azimuth) of fault zone head waves

Recent studies (e.g., Bulut et al., 2012; Allam et al., 2014) have shown that horizontal polarizations (arrival azimuths) of the FZHW and DWSA are quite different, and hence could be used as another diagnostic to distinguish them. We have examined polarizations of earthquakes that occurred along the

Parkfield section of the San Andreas Fault and were recorded by the PASO array in 2001-2002 (Li et al., 2013). The analysis procedure generally follows Bulut et al. (2012) and is briefly described here.

To utilize the polarization information on horizontal components, we plot the evolution of particle motion around the FZHW and DWSA window to identify how the polarization changes over time. We first filter the seismic data with a band-pass filter of 1-15 Hz. Next, we zoom in around the previously picked FZHW and DWSA (Zhao et al., 2010), and plot the particle motions using the two horizontal components for a total of 8 windows with a window length of 0.1 s (10 samples). To quantify changes in polarization, we calculate the polarization direction and linearity using the 2D covariance matrix as proposed by Jurkevics (1988):

$$\boldsymbol{S} = \frac{\boldsymbol{X}\boldsymbol{X}^{\boldsymbol{T}}}{N} = \begin{bmatrix} S_{EE} & S_{EN} \\ S_{NE} & S_{NN} \end{bmatrix} \text{ where } \boldsymbol{X} = [\boldsymbol{u_E}; \boldsymbol{u_N}].$$

corresponding to the amplitudes (either velocity or displacement) recorded on the E-W and N-S components. The eigenvalues λ_1 and λ_2 (assuming $\lambda_1 \geq \lambda_2$) represent the amplitudes of maximum and minimum principle axes of the polarization ellipse, respectively, while the eigenvectors ($\mathbf{u_1}$ and $\mathbf{u_2}$) correspond to the directions of the principle axes. The dominant direction of particle motion is given by $\mathbf{u_1}$ and the linearity is defined as $1- \lambda_2/ \lambda_1$.We compute these two parameters using a 0.1-s moving window centered on each data point.

Ideally, we would expect to observe the DWSA polarized in the source-receiver direction while the FZHW would likely be polarized at a different angle, related to the fault strike. Figure 7 shows the particle motions of the horizontal components at station CLIF that were generated by a magnitude 3.8 event (35.862° N, 120.417° W, 9.5 km depth) that occurred on Sep 6, 2002. A clear change in the polarization is observed: a nearly N-S polarization direction for the FZHW and a NW-SE polarization direction for the DWSA. Figure 8 shows polarization parameters of the FZHW and DWSA in Figure 7. The results are generally consistent with the visual inspection in Figure 7, but provide additional interesting features. First, the duration of stable polarization of the DWSA is rather short (~0.3 s) and is likely disturbed by P wave coda and/or scattered waves. Secondly, both polarization direction and linearity show abrupt changes when approaching the transition between different types of signals (namely noise - FZHW, FZHW - DWSA, DWSA - scattering phases).

We have expanded the polarization analysis to the 2002 data recorded by PASO network, for which the FZHW and DWSA arrivals were picked by Zhao et al. (2010). Because FZHW's were only recorded on the slow side of the fault, we only examine the polarizations at stations within 5 km on the NE side of the SAF. In addition, we require that the source-receiver distance to be long enough (e.g., ~20 km) so that the FZHW and DWSA are well separated. A total of 366 event-station pairs are selected. However, the results from the expanded data set show that the polarizations of the FZHW and DWSA display much more complicated patterns than originally expected. We find that a significant fraction of the station-event pairs in which FZHW's are identified using vertical components show diffuse polarizations on the horizontal components. Figure 9 shows an example where both the FZHW and the DWSA are polarized along source-receiver direction (i.e., close to the SAF strike), although clear FZHW's can be observed on the vertical component (emergent phase, opposite polarity to the DWSA). In other cases, both the FZHW and DWSA are polarized in directions that are quite different from the source-receiver directions.

To further test the reliability of using polarization to identify FZHW and DWSA, we investigate the statistical distribution of the polarization parameters for the FZHW and DWSA for all 366 station-event pairs. First, we define the FZHW window from the FZHW arrival t_1 to the DWSA arrival t_2, and define the DWSA window starting from t_2 with the same window length as the FZHW window ($t_2 - t_1$). To obtain a stable polarization value, we further select the station-event pairs with $t_2 - t_1 > 0.1$ s in order to include at least 10 data points. Secondly, the horizontal components are rotated to the radial and transverse directions that are parallel and perpendicular to the source-receiver directions (Figure 10).

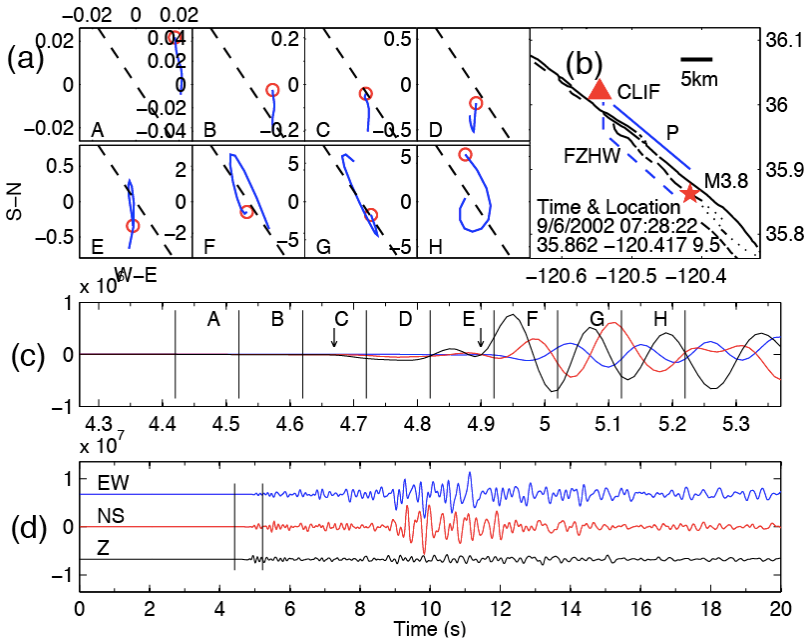

Figure 7. An example of polarization of the FZHW and DWSA. (a) Particle motion plot for 8 time windows around the FZHW and DWSA. (b) Locations of the earthquake and station CLIF. The black line denotes active. The solid and dashed blue lines mark the hypothetical ray path of the DWSA and FZHW. (c) A zoomed-in plot of the three-component seismograms at station CLIF around the FZHW and DWSA. (d) 20-s-long three-component seismograms at station CLIF.

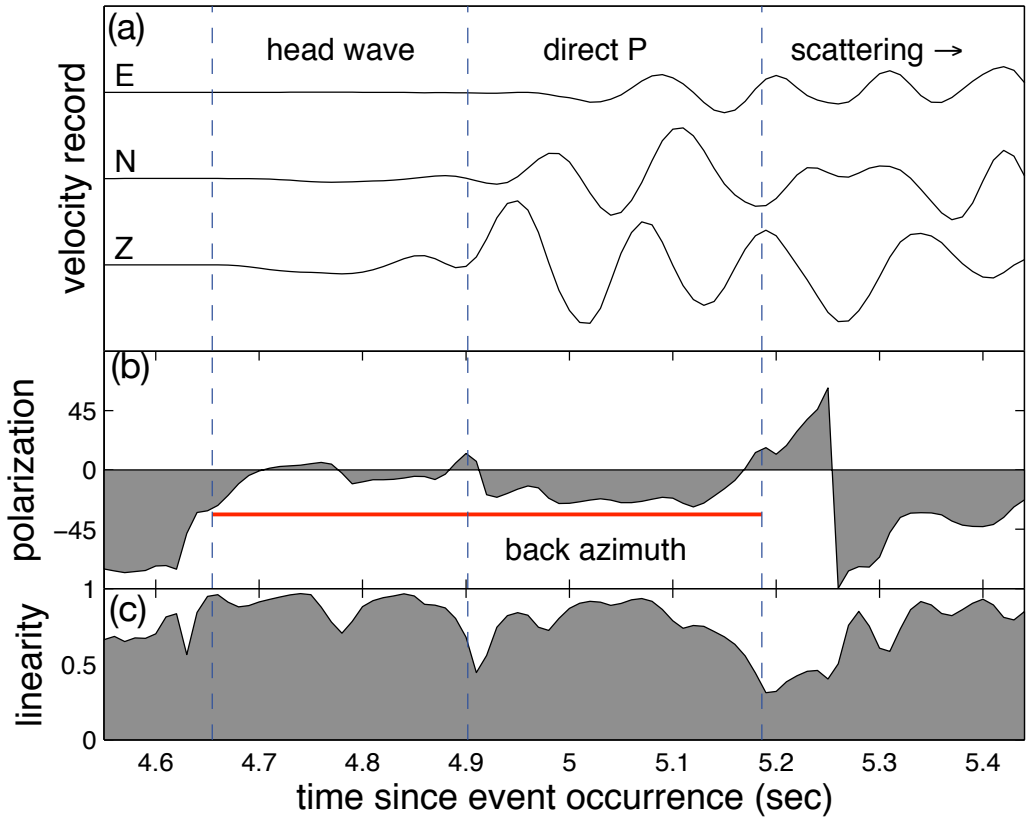

Figure 8. Quantitative measurements of FZHW and DWSA (P) polarizations using the same station-event pair in Figure 7. The vertical dash lines mark the window of FZHW, DWSA, and scattered coda phases. (a) Three-component seismogram around FZHW and DWSA. (b) Polarization direction relative to north (positive is clockwise). A 0.1s window centered at each data point is used to compute polarization direction and linearity for that point. The red line denotes the source-receiver direction. (c) Polarization linearity at different times.

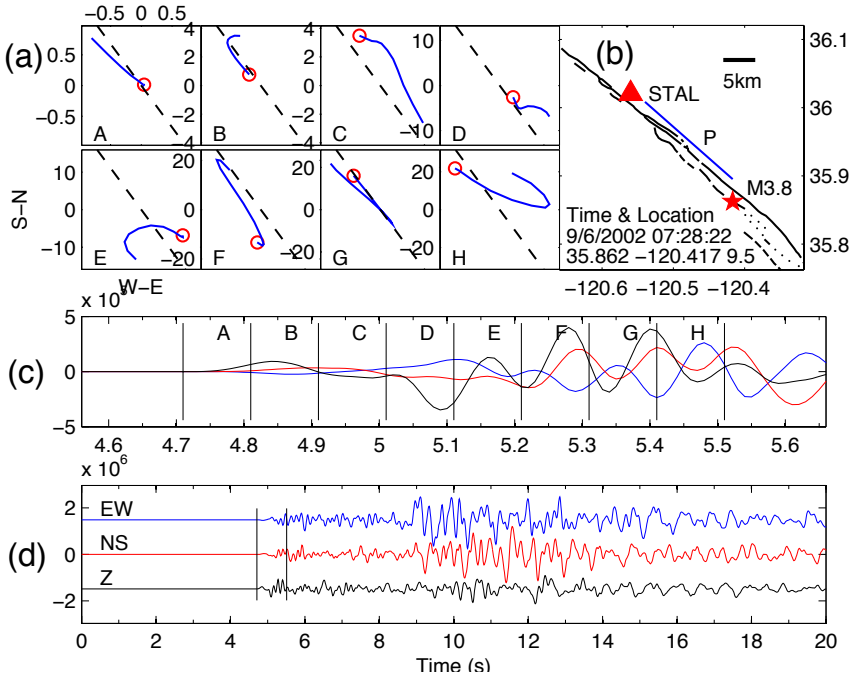

Figure 9. Similar to Figure 7, but the FZHW shows polarization similar to the DWSA, although the characteristics of the FZHW can be identified on the vertical components.

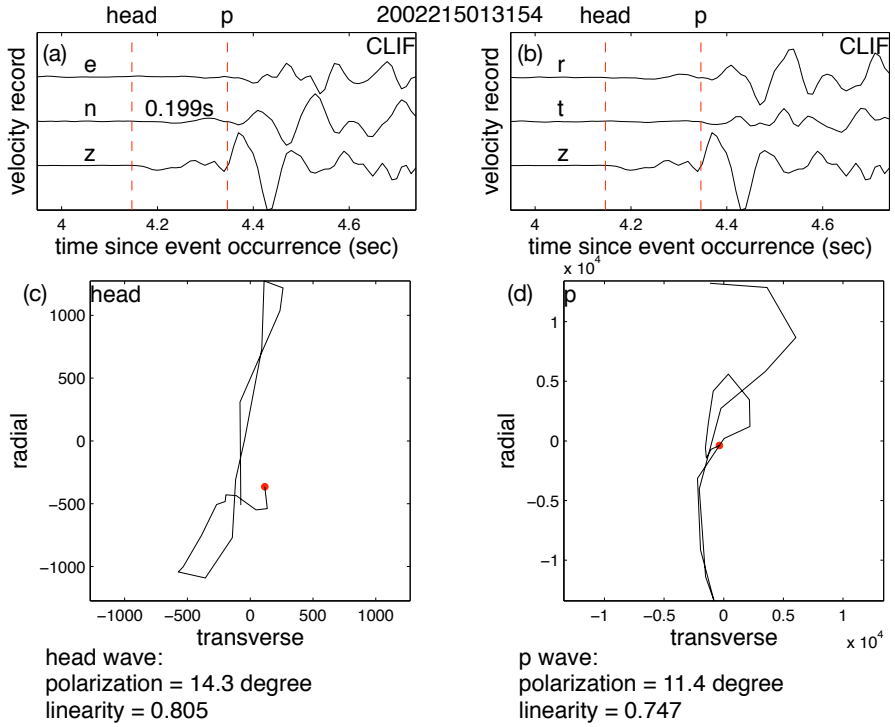

Figure 10. An example showing the polarization calculation procedure. (a) Original data around the FZHW and DWSA (P) arrivals. The duration of FZHW window is 0.199s. (b) Seismogram rotated to radial and transverse directions. (c) Particle motion when FZHW comes in. Red dot represent the starting point. (d) Particle motion when DWSA comes in. Note that the calculated polarization and linearity of both FZHW and DWSA are similar in this example, although the amplitudes are quite different.

Figure 11 shows the distribution of the DWSA and FZHW polarizations relative to the source-receiver directions. While both polarizations are clustered around the source-receiver directions (0°), we also observe a significant fraction of scattered measurements. The angle differences between the DWSA and FZHW polarization cannot be well distinguished. These results suggest that the polarizations of both the DWSA and FZHW are noisy and far from the theoretical prediction, making it difficult to utilize the information for any additional study.

There are several possible reasons that may explain these observations. First, because the seismic ray tends to bend towards vertical for increasing velocity with depth, the amplitudes of FZHW and DWSA on horizontal components are relatively low as compared to vertical components. Hence, the signal to noise ratio on the horizontal component is relatively low, and can be easily contaminated by noises, especially for the emergent FZHW phases. Secondly, for the Parkfield case, the theoretical difference of polarization angles of FZHW and DWSA is ~30°, assuming a 10% average velocity contrast. This relatively small angle is difficult to resolve, considering that the signal is weak and could be contaminated by noise. Finally, fault zones are strongly heterogeneous and the structures are usually very complicated, while the model for FZHW is relatively simple. Hence, polarizations of FZHW and DWSA may not be sensitive to the average velocity contrast, but are more affected by fault zone site effect or other structural complexities.

In summary, these observations suggest that while particle motions could be used to demonstrate the polarizations of the FZHW and DWSA for some events, they are not reliably observed for all source-receiver pairs. In addition, inclusion of arrival polarizations, as demonstrated in synthetic tests discussed below, did not provide further improvements to the velocity structure near the fault. Hence, the combination of FZHW and DWSA polarizations may not be as useful as previously thought.

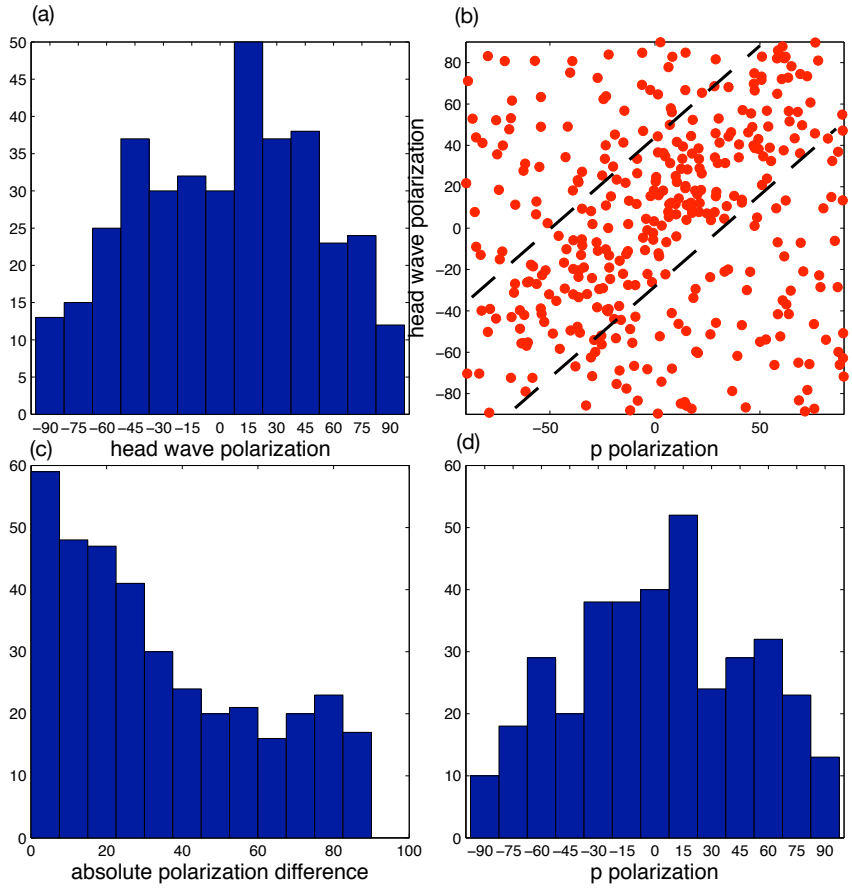

Figure 11. Statistical distribution of FZHW and DWSA (P) polarization. (a) Histogram of FZHW polarization. (b) DWSA polarization versus FZHW polarization. Note they are slightly correlated in the region that is bounded by the dash lines. (c) Histogram of absolute difference between FZHW and DWSA polarization. (d) Histogram of DWSA polarization. Note that all calculated polarization angles are related to the radial direction.

Research accomplished - arrival azimuth tomography

We have completed work solving for a 3D P-wave velocity model of the Parkfield region that utilizes existing P-wave arrival time data, including FZHW's, plus new data for DWSA's and FZHW's. This work has culminated in the publication of a manuscript in the Journal of Geophysical Research (Bennington et al., 2013), summarized above. We have expanded on that work by modifying our seismic tomography algorithm to incorporate arrival azimuths. For every event-station pair in our data set, the arrival azimuth partial derivative at each node in the model is calculated using a "brute force" approach. In this approach, for a given event-station pair, the arrival azimuth at the station is calculated using the current velocity model. The slowness at each node in the vicinity of the ray path in the current velocity model is then independently perturbed by the same change in slowness (the reciprocal of velocity) Δu and the arrival azimuth for the current event-station pair is recomputed with this perturbation. For the current event-station pair, the arrival azimuth partial derivative at node i is then estimated as $\partial\alpha/\partial u_i = \Delta\alpha/\Delta u_i$, where $\partial\alpha/\partial u_i$ is the partial derivative at node i, Δu_i is the perturbation in slowness at node i, and $\Delta\alpha$ is the calculated change in the arrival azimuth due to the slowness perturbation at node i. For each event-station pair, this procedure is repeated at every node in the velocity model that is within a specified distance of the ray path to obtain the arrival azimuth partial derivatives for that event-station pair.

Synthetic tests were carried out to test the utility of incorporating arrival azimuths into an inversion for velocity structure. To determine a reasonable Δu to perturb each node by, we determined the arrival azimuth partial derivatives at 28 of the inversion grid nodes (5% of the total number of nodes) for a range of applied slowness perturbations (0.005 to 0.04 s/km). At each node examined, for $\Delta u \leq 0.01$ s/km, the resulting arrival azimuth partial derivatives were essentially constant. Thus, we selected $\Delta u = 0.01$ s/km. For testing, we created a low velocity sandwich model (Figure 12) as our synthetic model. From this model, we generated synthetic FZHW, DWSA, and "normal" P-wave arrival time data (both absolute and differential travel times). Synthetic arrival azimuth data (for P-wave first arrivals, FZHW's, and DWSA's) were also generated for every event-station pair, where they exist.

The synthetic arrival time data were inverted using a 1D starting model with Vp = 5.25, 5.31, 5.37, 5.44, and 5.50 km/s at Z = 0, 3, 7, 11, and 16 km, respectively. Figure 13 a, c, and e show the difference between the recovered (Figure 13 b, d, and f) and synthetic (Figure 12) Vp models. Differences between the two are minimal (< 0.1 km/s) at $X \leq -0.75$ km and $X > 4$ km demonstrating that the arrival time data alone do an excellent job recovering the velocity in these regions. The low velocity sandwich layer we recover is ~0.6 km/s too fast.

Next, we inverted the arrival azimuth data only using the model constrained by arrival time data as our starting model. Thus, any changes in the recovered model were due to the inclusion of the arrival azimuth data. The resulting model is shown in Figure 14. Again, we compute differences (Figure 14 a, c, and e) between the recovered (Figure 14 b, d, and f) and the synthetic Vp model (Figure 12). At the low velocity sandwich layer, these difference plots (Figure 14 a, c, and e) are approximately the same as those in Figure 13 a, c, and e. From this we infer that the inclusion of arrival azimuth data neither improves nor degrades the recovered Vp model for this region of the model. In fact, it appears that the azimuth data do not further constrain this part of the model. At $X \leq -0.75$ km, relative to the arrival-time-constrained

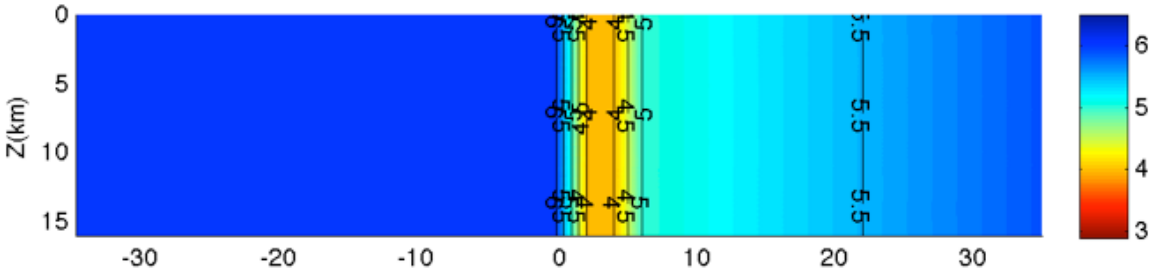

Figure 12. Synthetic velocity model with low velocity "sandwich" layer (low Vp of 4 km/s).

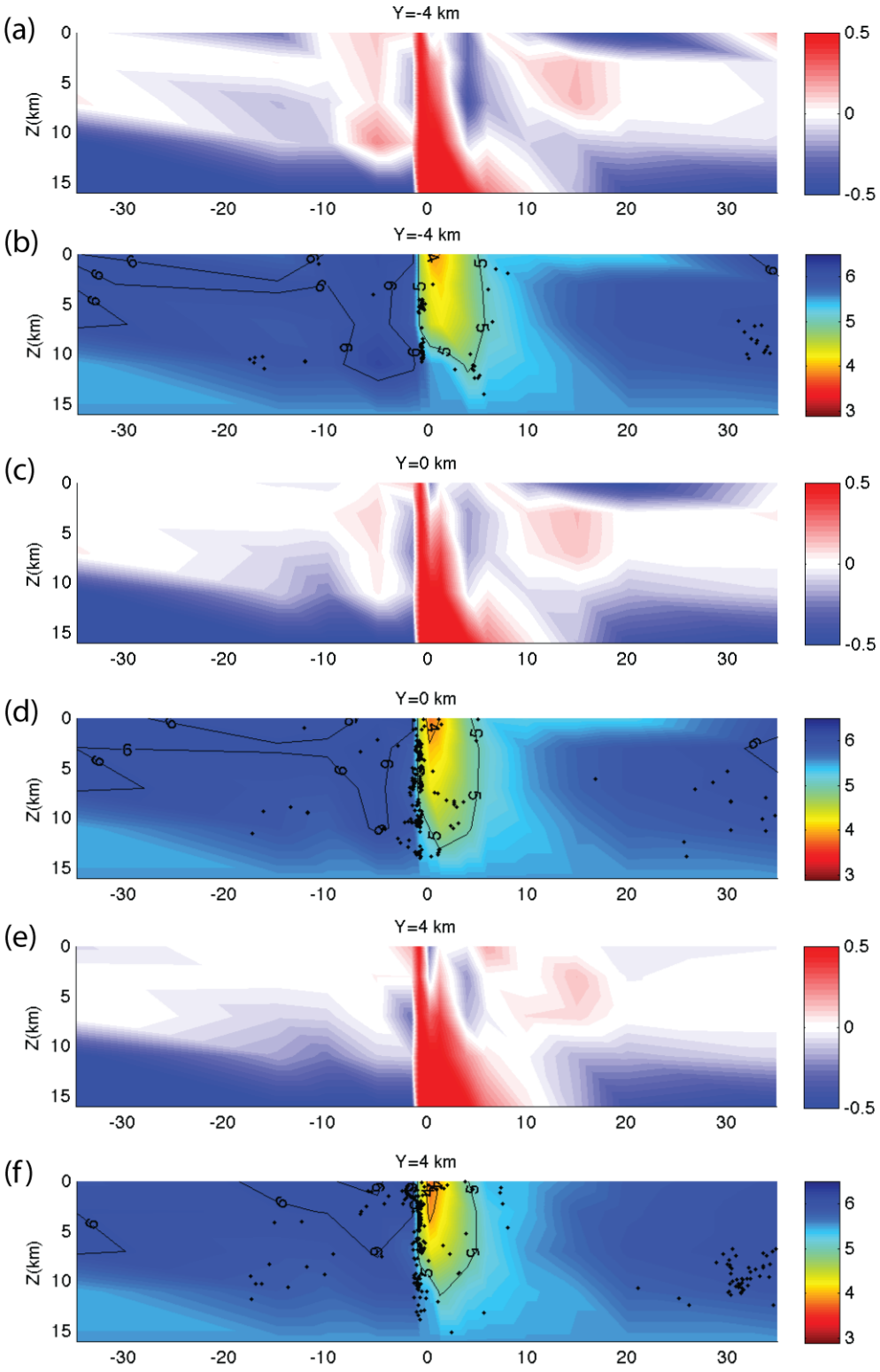

Figure 13. Differences between the recovered (inverted using arrival time data only) and synthetic Vp models are shown in (a), (c), and (e). The recovered models from inversion of the arrival time data are shown in (b), (d), and (f), which can be compared to Figure 12.

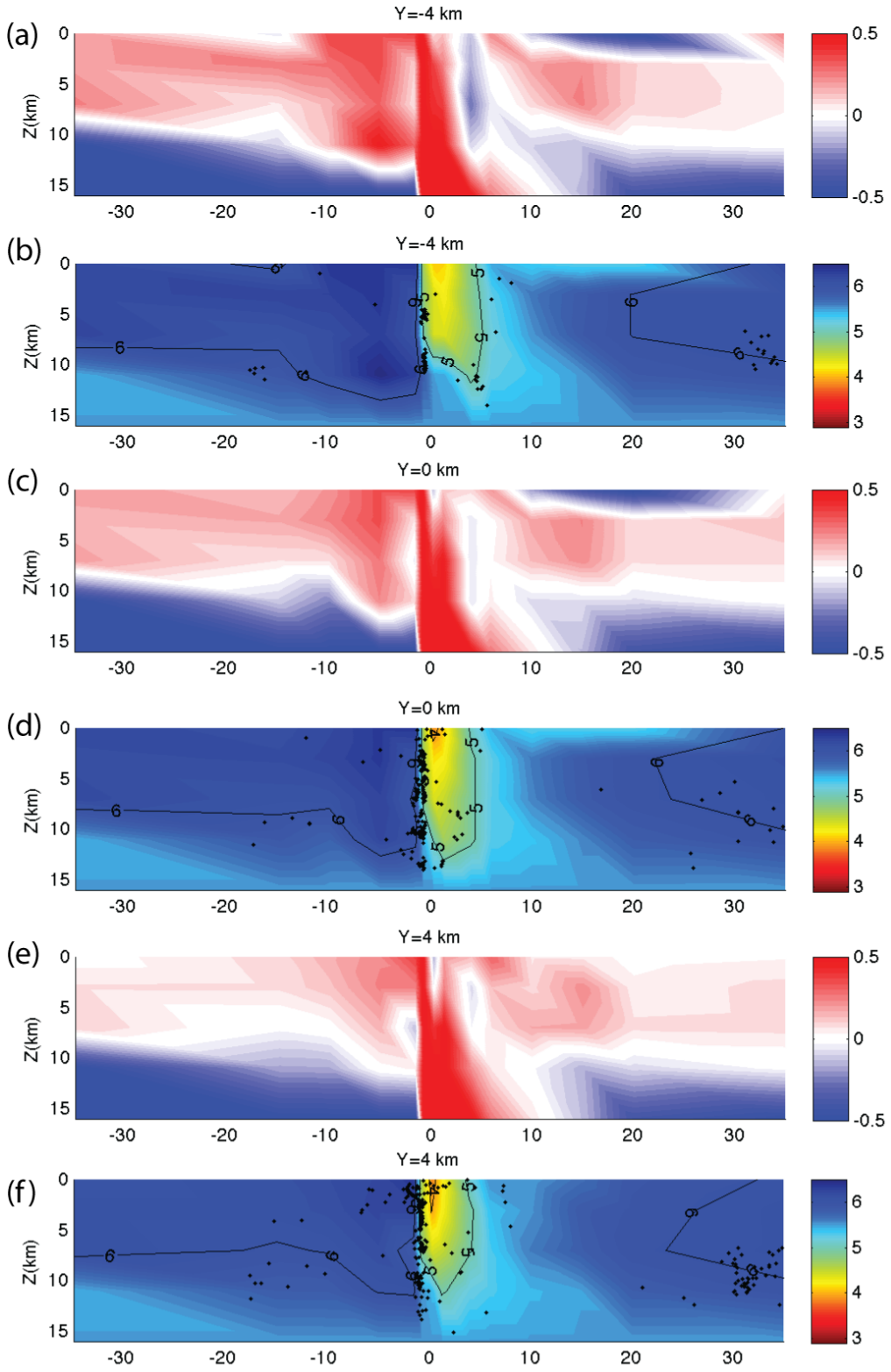

Figure 14. Differences between the recovered (inverted using arrival azimuth data only) and synthetic Vp models are shown in (a), (c), and (e). The recovered models from inversion of the arrival azimuth data only are shown in (b), (d), and (f), which can be compared to Figure 12.

model (Figure 13), changes to the Vp model from inversion of the arrival azimuth data produce a model that is ~0.6 km/s too fast relative to the synthetic model. Thus, in this part of the model, incorporation of the arrival azimuth data yields a model that is farther from the input synthetic model than that from arrival times alone. This is also true, although to a lesser extent, at X > 4 km, where incorporation of the arrival azimuth data yields a models that is ~0.2 km/s too fast relative to the synthetic model.

To determine the reason for this degradation of the recovered model including the arrival azimuth data, we examine the magnitude of calculated arrival azimuth partial derivatives for a number of FZHW/DWSA pairs. Instead of looking at the arrival azimuth partial derivatives that have been calculated in the 3D space (those partials associated with the inversion for the model in Figure 12), we simplify the matter by calculating the partial derivatives associated with a 2D model space where events are located at Z = 0 km. The results (Figure 15) are plotted in the X-Y model space and show the absolute values of the arrival azimuth partial derivatives for an example FZHW and DWSA. Comparing the magnitude of these partials, we see that the FZHW case has 9 non-zero partial derivatives with absolute values ranging from ~2 to 120 whereas the DWSA case has only 4 non-zero partial derivatives ranging from ~1 to 40. The greater number of non-zero FZHW partial derivatives and their larger size demonstrates that the FZHW has a stronger contribution to the solution. In addition, we see that the largest partial derivatives for the FZHW's are located at X ≤ -0.75 km, indicating why the largest changes to the Vp model are occurring almost entirely in that area of the model. For our goal of sharpening the image of the velocity contrast, the difficulty is that the FZHW partial derivative values are spread along the length of the ray path on the fast side of the fault. Therefore, including the FZHW and DWSA data does not allow for a localization of the velocity contrast to the immediate vicinity of the fault near the source or receiver, and instead will smear velocity perturbations over a larger region.

Conclusions

We incorporated a set of FZHW and DWSA arrival times into the existing set of first-arrival time data for the Parkfield region, and used the combined dataset to obtain an updated Vp model for the region. We compared our final Vp model to that of Thurber et al. (2006) and found that the main features of the two models generally agree well. However, contours of high and low velocity on opposite sides of the fault move closer to the fault and align nearer to and/or along zones of seismicity, yielding an overall increase in the across-fault velocity contrast relative to both our starting model and the final model of Thurber et al. (2006). Looking along strike, three pronounced velocity contrast regions are observed: strong positive velocity contrasts (i.e., NE side slow) both NW of the 1966 Parkfield earthquake and SE of the 2004 Parkfield earthquake and a strong negative velocity contrast (i.e., NE side fast) between the 1966 and 2004 events. Similar velocity contrasts were imaged by Thurber et al. (2006), however, the inclusion of FZHW and DWSA data increases the spatial dimensions and amplitudes of the across-fault velocity contrasts (both negative and positive) by as much as 5% relative to our starting model and as much as 10% relative to Thurber et al. (2006). We find that the area of the strong negative velocity contrast in our model agrees well with the lateral extent of peak coseismic slip estimated from both geodetic and strong motion studies. Three of the coseismic slip models examined place main shock slip from 5 to 10 km depth, whereas our negative velocity contrast exists from 7 to 15 km. One coseismic slip model (Kim and Dreger, 2008) places the two main peak slip patches within the main negative velocity contrast and a smaller negative velocity contrast located to the SE. This suggests that the negative velocity contrast played a role in defining the rupture patch for the 2004 Parkfield earthquake. Velocity contrasts at the 2004 Parkfield earthquake hypocenter suggest bilateral rupture propagation, as was observed during the event. Velocity contrasts at the 1966 Parkfield hypocenter also suggest bilateral rupture, but given the velocity strengthening behavior of the creeping section of the SAF to the NW, it is not surprising that rupture propagated only to the SE during that event.

In summary, we have succeeded in incorporating FZHW's and DWSA's in a formal tomographic inversion for velocity structure. Our results show that this approach produces a clear sharpening of the velocity contrast across the fault in the 3D tomographic model. Furthermore, comparison of the resulting velocity contrast to other geophysical observations shows that the velocity contrast variations appear to be

directly related to the variations in fault slip behavior. Unfortunately, the addition of arrival azimuth data to the inversion was ineffective due to the non-localized sensitivity of the arrival azimuths to velocity model perturbations.

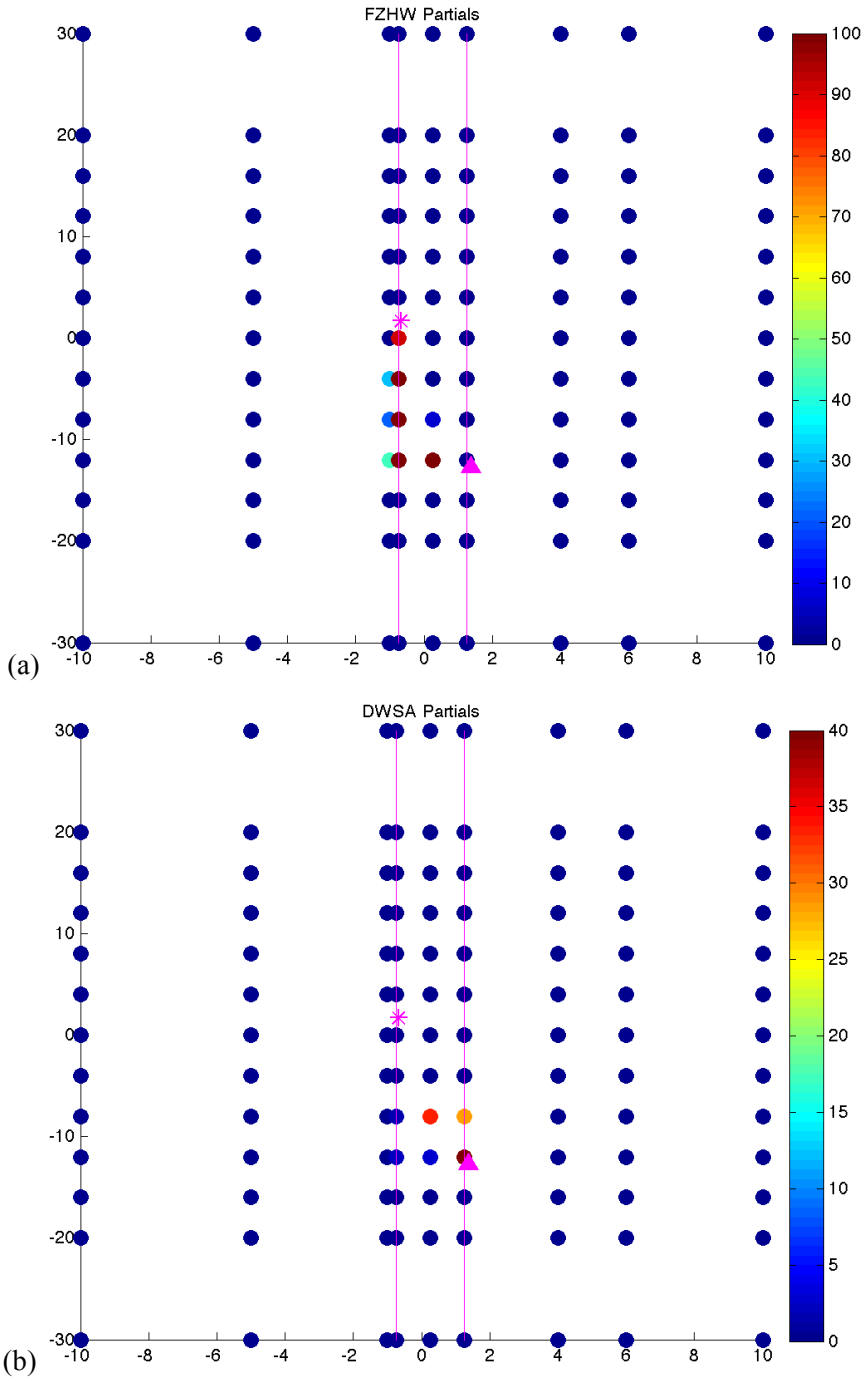

Figure 15. For a particular event-station pair, we show the magnitude of the (a) FZHW and (b) DWSA arrival azimuth partial derivatives at each node in the 2D model space. The red asterisk and triangle denote the event and station location, respectively. Purple lines outline the low velocity sandwich region of the model. Note that the distance scales differ in the two coordinate directions.

References

Ampuero, J.-P. and Y. Ben-Zion (2008), Cracks, pulses and macroscopic asymmetry of dynamic rupture on a bimaterial interface with velocity-weakening friction, Geophys. J. Int., doi: 10.1111/j.1365-246X.2008.03736.x.

Allam, A. A., Y. Ben-Zion and Z. Peng (2014), Seismic imaging of a bimaterial interface along the Hayward fault, CA, with fault zone headwaves and direct P arrivals, *Pure App. Geophys.*, in press, doi: 10.1007/s00024-014-0784-0.

Andrews, D. J. and Y. Ben-Zion (1997), Wrinkle-like slip pulse on a fault between different materials, J. Geophys. Res., 102, 553-571.

Barnhart, W. D., and R. B. Lohman (2010), Automated fault model discretization for inversions for coseismic slip distributions, J. Geophys. Res., 115, B10419, doi:10.1029/2010JB007545.

Ben-Zion, Y. (1989), The response of two joined quarter spaces to SH line sources located at the material discontinuity interface, Geophys. J. Int., 98, 213-222.

Ben-Zion, Y. (1990), The response of two half spaces to point dislocations at the material interface, Geophys. J. Int., 101, 507-528.

Ben-Zion, Y. (2006), Comment on "Material contrast does not predict earthquake rupture propagation direction" by R. A. Harris and S. M. Day, Geophys. Res. Letters, 33, L13310.

Ben-Zion, Y., and K. Aki (1990), Seismic radiation from an SH line source in a laterally heterogeneous planar fault zone, Bull. Seism. Soc. Am., 80, 971-994.

Ben-Zion, Y., S. Katz, and P. Leary (1992), Joint inversion of fault zone head waves and direct P arrivals for crustal structure near major faults, J. Geophys. Res., 97, 1943-1951.

Ben-Zion, Y. and P. Malin (1991), San Andreas fault zone head waves near Parkfield, California, Science, 251, 1592-1594.

Bennington, N. L., C. Thurber, Z. Peng, H. Zhang, and P. Zhao (2013), Incorporating fault zone head wave and direct wave secondary arrival times into seismic tomography: Application at Parkfield, California, J. Geophys. Res., 118, 1-7, doi:10.1002/jgrb.50072.

Bennington, N., C. Thurber, K. Feigl, and J. Murray-Moraleda (2011), Aftershock distribution as a constraint on the geodetic model of coseismic slip for the 2004 Parkfield earthquake, Pure App. Geophys., 168, 1553-1565.

Brocher, T. (2008), Compressional and shear-wave velocity versus depth relations for common rock types in northern California, Bull. Seism. Soc. Am., 98, 950-968.

Bulut, F., Y. Ben-Zion and M. Bonhoff (2012), Evidence for a bimaterial interface along the Mudurnu segment of the North Anatolian fault zone from polarization analysis of P waves, Earth Planet. Sci. Lett., in press, doi:10.1016/j.epsl.2012.02.001.

Custódio, S., M. Page, and R. Archuleta (2009), Constraining earthquake source inversions with GPS data: 2. A two-step approach to combine seismic and geodetic data sets, J. Geophys. Res, 114, B01315.

Eberhart-Phillips, D. and A. J. Michael (1993), Three-dimensional velocity structure, seismicity, and fault structure in the Parkfield region, central California, J. Geophys. Res., 98, 15,737-15,758.

Harris, R., and S. Day (2005), Material contrast does not predict earthquake rupture propagation direction, Geophys. Res. Letters, 32, doi: 10.1029/2005GL023941.

Haslinger, F., and E. Kissling (2001), Investigating effects of 3-D ray tracing methods in local earthquake tomography, Phys. Earth Planet. Int., 123, 103-114.

Hickman, S., M. Zoback, W. Ellsworth, N. Boness, P. Malin, S. Roecker, and C. Thurber (2007), Structure and properties of the San Andreas Fault in central California: Recent results from the SAFOD experiment, Scientific Drilling, Special Issue No. 1, 29-32, doi:10.0/iodp.sd.s01.9.007.

Hickman, S., M. Zoback, W. Ellsworth, J. Chester, F. Chester, J. Evans, D. Moore, D. Kirschner, A. Scleicher, B. van der Pluijm, and J. Solum (2008), Structure and composition of the San Andreas fault in central California: Recent results from SAFOD sample analyses, EOS Trans. AGU, 89, Fall Meeting Supplement, abtract T53F-01.

Jurkevics, A. (1988), Polarization analysis of three component array data, Bull. Seismol. Soc. Amer., 78, 1725 -1743.
Kim, A. and D. Dreger (2008), Rupture process of the 2004 Parkfield earthquake from near-fault seismic waveform and geodetic records, J. Geophys. Res, 113, B07308.
Legliné, O., and J. Got (2011), Rupture directivity of microearthquake sequences near Parkfield, California, Geophys. Res. Letters, 38, L08310, doi:10.1029/2011GL047303.
Lewis, M. A, Y. Ben-Zion and J. McGuire (2007), Imaging the deep structure of the San Andreas Fault south of Hollister with joint analysis of fault-zone head and direct P arrivals, Geophys. J. Int., 169, 1028-1042, doi: 10.1111/j.1365-246X.2006.03319.x.
Li, Z., Z. Peng, P. Zhao, N. L. Bennington, and C. Thurber (2013), Polarization analysis of fault zone head waves along the Parkfield section of the San Andreas Fault, Seismol. Res. Lett., 84(2), 379.
McGuire, J., and Y. Ben-Zion (2005), High-resolution imaging of the Bear Valley section of the San Andreas fault at seismogenic depths with fault-zone head waves and relocated seismicity, Geophys. J. Int., 163, 152-164.
McLaughlin, R. J., W. V. Sliter, D. H. Sorg, P. C. Russell, and A. M. Sarna-Wojcicki (1996), Large-scale right-slip displacement on the east San Francisco Bay region fault system, California: implications for location of late Miocene to Pliocene Pacific plate boundary, Tectonics 15, 1-18.
Thurber, C., and D. Eberhart-Phillips (1999), Local earthquake tomography with flexible gridding, Comp. & Geosci., 25, 809-818.
Thurber, C., S. Roecker, H. Zhang, S. Baher, and W. Ellsworth (2004), Fine-scale structure of the San Andreas fault and location of the SAFOD target earthquakes, Geophys. Res. Lett., 31, L12S02.
Thurber, C., H. Zhang, F. Waldhauser, J. Hardebeck, A. Michael, and D. Eberhart-Phillips (2006), Three-dimensional compressional wavespeed model, earthquake relocations, and focal mechanisms for the Parkfield, California, region, Bull. Seismol. Soc. Am., 96, S38-S49.
Toomey, D., and Foulger, G. (1989), Tomographic inversion of local earthquake data from the Hengill-Grensdalur central volcano complex, Iceland, J. Geophys. Res., 94, 17497-17510.
Um, J., and C. Thurber (1987), A fast algorithm for two-point seismic ray tracing, Bull. Seism. Soc. Am., 77, 972-986.
Waldhauser, F., W. Ellsworth, D. P. Schaff, and A. Cole (2004). Streaks, multiplets, and holes: High-resolution spatio-temporal behavior of Parkfield seismicity, Geophys. Res. Lett. 31, L18608, doi:10.1029/2004GL020649.
Zhang, H. and C. Thurber (2003), Double-difference tomography: The method and its application to the Hayward Fault, California, Bull. Seismol. Soc. Am., 93, 1875-1889; DOI: 10.1785/0120020190.
Zhang, H., C. Thurber, and P. Bedrosian (2009), Joint inversion for Vp, Vs, and Vp/Vs at SAFOD, Parkfield, California, Geochem. Geophys. Geosyst., 10, Q11002, doi:10.1029/2009GC002709.
Zhao, P., and Z. Peng (2008), Velocity contrast along the Calaveras fault from analysis of fault zone head waves generated by repeating earthquakes, Geophys. Res. Lett., 35, L01303, doi:10.1029/ 2007GL031810.
Zhao, P., Z. Peng, Z. Shi, M. Lewis, and Y. Ben-Zion (2010), Variations of the velocity contrast and rupture properties of M6 earthquakes along the Parkfield section of the San Andreas fault, Geophys. J. Int., 180, 765-780, 10.1111/j.1365-246X.2009.04436.x.

Bibliography of published work

Bennington, N. L., C. Thurber, Z. Peng, H. Zhang, and P. Zhao (2013), Incorporating fault zone head wave and direct wave secondary arrival times into seismic tomography: Application at Parkfield, California, J. Geophys. Res., 118, 1-7, doi:10.1002/jgrb.50072.
Bennington, N. L., C. H. Thurber, Z. Peng, and P. Zhao (2012), The incorporation of fault zone head wave and direct wave secondary arrival times and arrival polarizations into seismic tomography: Application to the Parkfield, California area, Fall AGU Meeting, abstract S31C-08.
Li, Z., Z. Peng, P. Zhao, N. L. Bennington, and C. Thurber (2013), Polarization analysis of fault zone head waves along the Parkfield section of the San Andreas Fault, Seismol. Res. Lett., 84(2), 379.